



Widefield wavefront sensor for multidirectional peripheral retinal scanning

DIBYENDU PUSTI,^{1,2}  CHLOE DEGRE KENDRICK,^{1,2} YIFEI WU,² QIUZHI JI,^{3,4} HAE WON JUNG,^{1,3} AND GEUNYOUNG YOON^{1,2,*} 

¹College of Optometry, University of Houston, Houston, TX 77204, USA

²Flaum Eye Institute, University of Rochester, Rochester, NY 14623, USA

³Institute of Optics, University of Rochester, Rochester, NY 14627, USA

⁴School of Optometry, Indiana University, Bloomington, IN 47405, USA

*gyoon2@Central.UH.Edu

Abstract: The quantitative evaluation of peripheral ocular optics is essential in both myopia research and the investigation of visual performance in people with normal and compromised central vision. We have developed a widefield scanning wavefront sensor (WSWS) capable of multidirectional scanning while maintaining natural central fixation at the primary gaze. This Shack-Hartmann-based WSWS scans along any retinal meridian by using a unique scanning method that involves the concurrent operation of a motorized rotary stage (horizontal scan) and a goniometer (vertical scan). To showcase the capability of the WSWS, we tested scanning along four meridians including a 60° horizontal, 36° vertical, and two 36° diagonal scans, each completed within a time frame of 5 seconds.

© 2023 Optica Publishing Group under the terms of the [Optica Open Access Publishing Agreement](#)

1. Introduction

Myopia is a global concern, affecting more than 30% of the world's population and up to an alarming rate of 92% of the youth population in south & east Asian countries [1,2]. Besides a substantial socio-economic burden, high myopia increases the risk of blindness through associated ocular pathologies like retinal disorders, glaucoma, and cataract [3–9]. Acknowledging the significant need for myopia control, recent studies have widely discussed relative peripheral refraction as a critical parameter to comprehend the underlying causes of myopia progression and to develop prevention strategies. The study of peripheral refraction came to the limelight when Rempt et al. in 1971 used peripheral refraction profiles to predict future myopia incidence in young pilots [10,11]. The important contribution of the peripheral retina to visual system development was established by an animal study conducted by Smith et al., which showed emmetropization can continue even after central retinal laser ablation [12]. Studies conducted through cross-sectional research have suggested that myopic eyes are more likely to experience relative hyperopic peripheral defocus, while emmetropic and hyperopic eyes tend to have a relatively myopic periphery [13–18]. Further investigations in animal models and human eyes supported the hypothesis that peripheral hyperopic defocus may be responsible for retinal elongation or the development of axial myopia [12,19–21]. On the contrary, recent longitudinal studies in children predicted that relative peripheral hyperopia may have little or no influence on the risk of myopia development [22–25]. Therefore, it is an ongoing debate whether the relative difference in peripheral refraction is a consequence or cause of myopia development [23–26]. Irrespective of this debate, many scientists and industries have gained interest in myopia control which has led to the development of corrective lenses that are designed to add plus power to the periphery with the goal of shifting relative peripheral refraction to be more myopic [27–31].

While these studies bring attention to the interaction between optically induced myopia and the peripheral retina, it is important to recognize that peripheral ocular optics are more complex than just defocus. Unlike the defocus-dominated central retina, the peripheral ocular optics

are primarily affected by astigmatism and non-rotationally symmetric higher-order aberrations (HOAs) like coma. These complex aberrations result in an anisotropic or directional optical blur. Therefore, myopia control lenses primarily designed to alter peripheral defocus also induce those asymmetric aberrations in the periphery, which then interact with the eye's native peripheral astigmatism and HOAs [32]. However, it is not well understood how the optical properties and retinal image quality of the eye across the visual field are altered by the aberrations induced by myopia control lenses when combined with the eye's native aberrations.

Evaluation of peripheral ocular optics is also important as it can affect visual performance in individuals with normal or compromised central vision [33,34]. The impact of peripheral aberrations on daily activities such as reading, driving, walking, and playing sports is also of great interest [35,36]. In addition, research has explored peripheral aberrations in individuals with pseudophakia [37,38] or keratoconus [39], as well as how peripheral optics influence contrast sensitivity [40], accommodation [41], and pupil size variation [42]. Overall, there is a growing body of research that highlights the importance of evaluating peripheral ocular optics. Consequently, the creation of an optical tool capable of measuring peripheral eye aberrations represents a crucial step in conducting both basic and clinical research, particularly in comprehending myopia mechanisms and designing optical tactics to prevent and decelerate its progression.

In the last decades, several approaches have been developed to measure peripheral ocular optics with Shack-Hartmann (SH) wavefront sensors. Currently, several methods employ either continuous or discrete point scanning techniques [43–49]. While current peripheral wavefront scanning sensors are an exciting development in this field, they still have some limitations such as relatively small scanning ranges [47] and limited scanning meridians [46,48]. Additionally, some systems require either eccentric fixation through an eye or a head turn to measure the peripheral aberrations. Therefore, the goal of the study was to develop a robust scanning wavefront sensor equipped with a new scanning mechanism that overcomes these limitations. This article presents a custom-built Widefield Scanning Wavefront Sensor (WSWS) with multidirectional scanning capability while maintaining natural eye fixation at primary gaze.

2. Methodology

2.1. Subjects' demographics

Twenty-two healthy young participants (10 females and 12 males) enrolled in the study, aged between 19 and 35 years. All the subjects met the study inclusion criterion and had healthy ocular integrity with no history of ocular pathology, surgery, or medication. The majority of these subjects were university students, including our lab members. Overall, the subject population had an average refraction of -1.98 ± 3.06 D (range: +3.96 D to -7.46 D). The study was conducted in accordance with the principles outlined in the Declaration of Helsinki and received ethical approval from the Institutional Review Board for human subject research at the University of Rochester, Rochester, NY, USA.

2.2. Optical design

The WSWS was designed to measure ocular aberrations at various eccentricities across any meridian of the eye. Figure 1 shows a schematic diagram of the instrument's optical system comprising both illumination and measuring optics and utilizing an 850 nm laser diode source with a 400 μ m pinhole. The laser power entering the eye is 40 μ W, which is over ten times lower than the ANSI national laser safety standard [50]. The near-infrared light is reflected by a 45-degree-oriented pellicle beam-splitter (BS1) before entering the eye. The reflected backlight from the retina passes through BS1 and the 4-F telescopic system, consisting of Lens 1 ($f = 100$ mm) and Lens 2 ($f = 75$ mm), resulting in 25% pupil demagnification. The transmitted light is

then reflected by another beam-splitter (BS2) and enters the SH wavefront sensor, which uses a micro-lenslet array with a pitch of $300\ \mu\text{m}$ and $4.5\ \text{mm}$ focal length placed at the pupil conjugate. Two identical CMOS sensors (MQ013RG-e2, Ximea, Inc.) were used for wavefront sensing and pupil imaging. The sensors have a resolution of 1280×1024 pixels, an active sensor dimension of $6.9 \times 5.5\ \text{mm}$ (pixel size: $5.4\ \mu\text{m}$), and high sensitivity for the near-infrared range. A ring LED of wavelength $950\ \text{nm}$ illuminates the pupil for alignment of the pupil center to the optical axis of the system, and the BS2 with a cutoff wavelength of $900\ \text{nm}$ separates the pupil illumination from the wavefront sensing light. A Maltese cross distance fixation target co-aligned with the optical system of the instrument allows for steady fixation, and a large cold mirror ($2\ \text{inches}$) redirects the Maltese cross to the subject's primary gaze fixation. A lens can be inserted into the open-view fixation optical path to correct for subjective refractive error and to control accommodation.

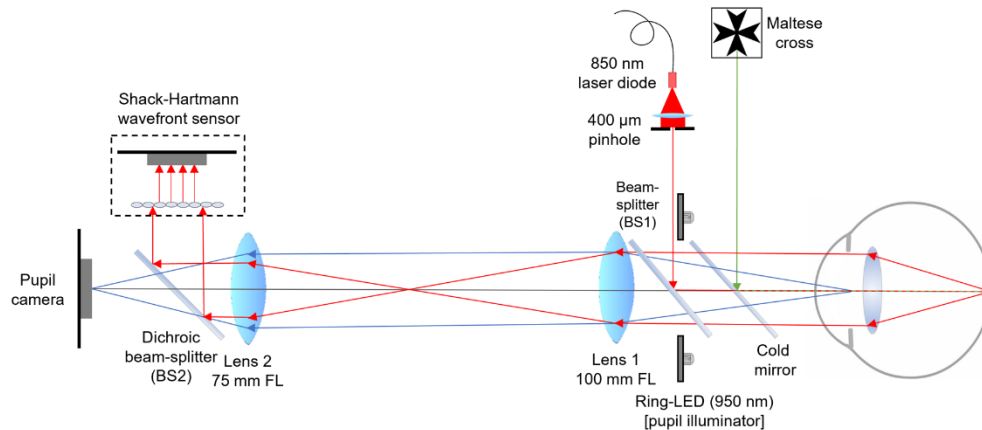


Fig. 1. Schematic diagram of the SH wavefront sensor's optical layout. The beam-splitter (BS1) redirected collimated light with a wavelength of $850\ \text{nm}$ toward the eye. The reflected backlight from the eye followed the red-line pathway, passed through BS1, and then hit the 4-F telescopic system comprising lens 1, lens 2, and BS2. This system was used to relay the wavefront information from the entrance pupil to the lenslet array. The blue-line pathway represents IR light ($950\ \text{nm}$) from the ring-LED that illuminated the eye's pupil whose image was captured by the pupil camera. A cold mirror was used to maintain eye natural fixation during the peripheral scans.

2.3. Motorized scanning mechanism

In order to facilitate scanning along any meridian, the complete optical arm, excluding the fixation unit, was affixed to a rotational stage (R1) (4800 series, Velmex Inc., USA) as shown in Fig. 2. The fixation unit, which includes the cold mirror and Maltese cross, was always kept stationary to preserve central eye fixation. The high-capacity stage has an accuracy of 100 arc-seconds and repeatability of 1 arc-second. A goniometer (G1) consisting of another stepping motor (Y07-59D1-17155, Shinano Kenshi Co. Ltd, Japan) was mounted to R1 with its rotational axis perpendicular to the rotational axis of R1, so that G1 controlled the vertical rotation of the system while R1 controlled the horizontal rotation. The centers of rotation (CoR) of both motors were co-aligned to the center of the eye's pupil. This arrangement allowed the wavefront sensor to swing horizontally and vertically around the pupil center. Operation of individual motors allowed for horizontal and vertical scanning, while any diagonal meridian scan can be achieved by precisely synchronizing and combining the movement of both motors. In this study, 45° and 135° meridians were scanned by moving both motors at a similar speed, however, running one of the motors at a higher or lower speed compared to the other motor allows for scanning

of any other diagonal meridian. The pupil plane of the instrument was aligned to scan along four meridians: $\pm 30^\circ$ horizontally, $\pm 18^\circ$ vertically, and $\pm 18^\circ$ obliquely along the 45° and 135° meridians. The vertical and oblique scans were limited mainly by the obstruction of the incoming laser beam at extreme eccentricities by the anatomical structures around the eye (i.e. the eye socket and forehead), and the large size of the goniometer. R1, G1, and both CMOS sensors (pupil and wavefront) were precisely synchronized and controlled by custom-built software based on C++. [Visualization 1](#) provides a video demonstration of the scanning process conducted on one of our study participants.

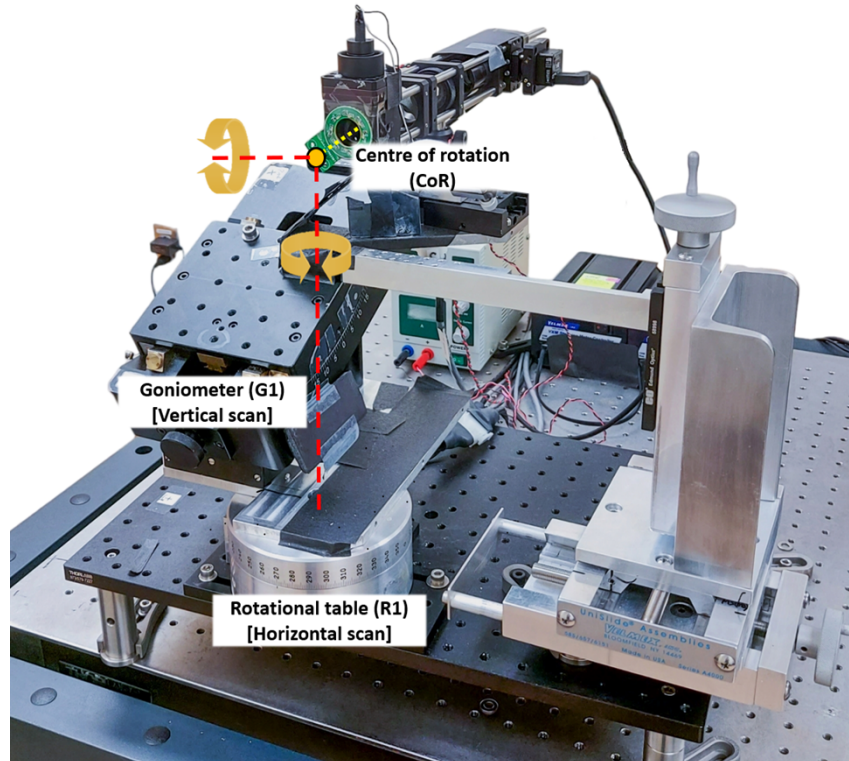


Fig. 2. Front view of the actual scanning wavefront sensor highlighting the motorized scanning mechanism. The SH wavefront sensor was mounted on the rotational stage consisting of a horizontal rotational table (R1) and a vertical goniometer (G1). The red dashed lines represent horizontal and vertical rotational axes. Both the rotational axes and optical axis (yellow dashed line) are coupled at the system's center of rotation (orange circle) corresponding to the eye's pupil center. The orange arrows represent the rotational path along the horizontal and vertical scans. The scanning process can be seen in the supplementary video (see [Visualization 1](#)).

The wavefront sensor used an exposure time of 10 ms, allowing real-time imaging of the pupil and spot pattern during each scan, which takes only 5 seconds to complete. The camera captures 20 frames per second, enabling the device to capture 1 degree/frame during the scanning process. However, we chose to process aberration data every 5° across horizontal, 6° across vertical and 4.5° across diagonal retinal eccentricities for aberration data analysis. The accuracy of the entrance pupil alignment with the center of rotation was assessed by imaging a paper reference target with a central crosshair and concentric circles at different eccentricities during the scanning process. No shift in pupil center position was observed throughout the scanning

range, and the center of the target remained sharply focused, indicating that the pupil plane was correctly matched to the CoR of both motors and that the pupil conjugate was not changed during the entire scan. It should be noted that with increasing scanning angles, the peripheral SH spot images became elliptical due to tangential imaging through the subject's pupil. Thus, the traditional Zernike fitting wavefront analysis process that is normally done on a circular pupil cannot be applied. Instead, we chose a modified version of the traditional Zernike fitting method using the 'circular subpart' approach by analyzing the central circular area from the ellipse as described by L Lundström et al [51].

2.4. Calibration of the wavefront sensor

The WFS was calibrated using high-precision lenses with optical powers ranging from -8 to +8 D. The calibration lenses were placed at the entrance pupil plane and a collimated laser of 635 nm that transmits through the lenses was measured for calibration. The wavefront images were captured and analyzed with custom-software for a 5.5 mm pupil. The defocus Zernike term from the lenses was correlated with the known power of the lenses. The slope and the regression line (r) of the calibration curve were measured to be 1.02 and 1.0 respectively, showing excellent correspondence. With magnification considered, the WFS can measure more than ± 8 D magnitude and differentiate less than a 0.05 D difference with 5.5 mm pupil diameter.

2.5. On-eye measurement procedure

Prior to measuring ocular aberrations, accommodation was paralyzed, and pupil dilation was achieved pharmacologically with one drop of each 1% tropicamide and 2.5% phenylephrine applied 30 minutes before measurement. The participants were instructed to focus on the center of a fixation target that corresponds to the optical axis of the sensor while scans were taken in all four directions. There was a short break between each meridional scan. The left eye of each participant was measured.

3. Results

3.1. Verification of peripheral measurements

A simplified model eye was created to assess the precision of the WSWS when evaluating peripheral aberrations. The model consisted of a doublet lens with a focal length of 30 mm (AC-254-030A from Thorlabs, Inc.) representing the cornea and lens of the eye, and a diffuser located at the focal point of the lens, mimicking the retina. Peripheral aberrations of the model eye, between 10 and 30 degrees of eccentricity in 5-degree increments, were measured using the WSWS. To validate the measured results, an optical ray tracing program (Zemax, LLC) was used to simulate the model eye by using the exact lens parameters provided by the manufacturer. Zemax simulations were performed at the same horizontal eccentricities at which the measurements were made, as shown in Fig. 3(A). Results from both the simulation and measurements were analyzed using a 5.5 mm pupil. For simplicity, we chose a flat diffuser unlike the curved retina in the real eye, which resulted in large defocus at the peripheral visual fields (up to 11.95 μm at 30°). Both simulation and model eye measurements indicated that defocus and astigmatism were the most significant aberrations, as plotted in Fig. 3(B) & 3(C). The nasal and temporal defocus (Z_2^0) and vertical astigmatism (Z_2^{-2}) showed good agreement with the theoretical values, especially closer to fovea. However, there was a small deviation that incur with eccentricity (max deviation: $Z_2^0=0.36 \mu\text{m}$ and $Z_2^{-2}=0.13 \mu\text{m}$ respectively at 30° visual field).

3.2. On-eye peripheral aberration measurement:

Peripheral scans were conducted in all 22 participants along the horizontal ($\pm 30^\circ$) and vertical meridians ($\pm 18^\circ$), while oblique scans ($\pm 18^\circ$) were only measured in eight subjects. On-eye

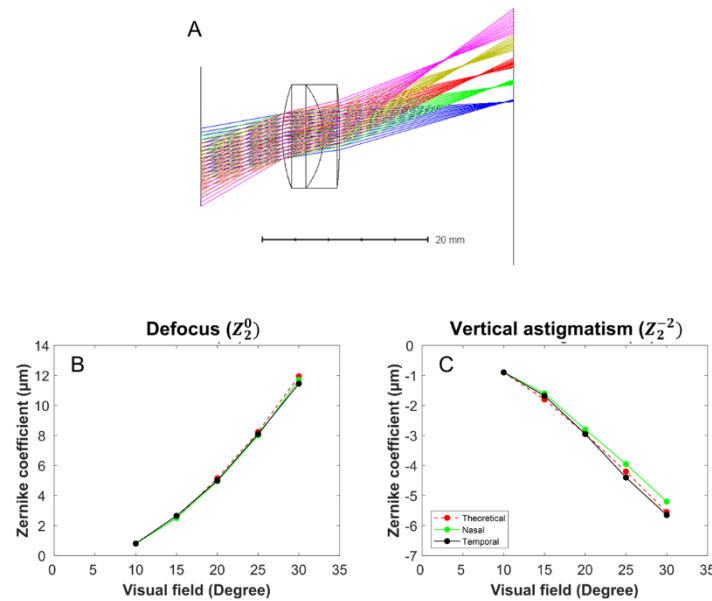


Fig. 3. The validation of the scanning wavefront sensor by comparing theoretical peripheral aberrations with model eye data. The theoretical peripheral aberration was determined by Zemax ray-tracing (A) through a doublet lens ($f = 30$ mm; AC-254-030A from Thorlabs, Inc.) with the exit pupil positioned on the lens back surface. The aberration was then measured with the WSWs for a 5.5 mm pupil. B and C illustrate the theoretical and measured peripheral defocus and astigmatism of nasal and temporal model eye, respectively. The Y-axis represents Zernike coefficient in microns and has varying scaling to highlight the validation comparison.

peripheral aberrations were calculated across the scanning range using a 5.5 mm pupil. Figure 4 depicts the lower-order aberrations (LOAs), which indicate defocus (Z_2^0) and astigmatism (Z_2^{-2} & Z_2^2) components across the four scanning directions. The standard deviation error bars represent inter-subject variability at each eccentric point. In our sample, the mean on-axis defocus at the fovea was $2.17 \pm 3.34 \mu\text{m}$. A slight deviation was noticed between foveal defocus values obtained from horizontal and vertical scans ($0.12 \pm 0.15 \mu\text{m}$) and between oblique scans ($0.27 \pm 0.34 \mu\text{m}$). We attribute this relatively small deviation to pupil decentration due to slight variations in the subjects' fixation during the different scans (refer to Fig. 4(A)). It is worth mentioning that the average foveal value in oblique scans varies from that in horizontal and vertical scans, primarily because of the difference in sample size.

To show the change in peripheral defocus relative to the foveal value, we subtracted the foveal value from each peripheral measurement point and presented the results in Fig. 4(B), where error bars represent the variance of peripheral defocus from the foveal value at each tested eccentricity. There was a gradual increase in relative hyperopic defocus towards both the temporal ($-0.61 \pm 0.48 \mu\text{m}$ at 30°) and nasal ($-0.73 \pm 0.80 \mu\text{m}$ at 30°) periphery with increasing horizontal eccentricity. Conversely, across the vertical meridian, relative myopic defocus gradually increased towards the inferior ($0.12 \pm 0.20 \mu\text{m}$ at 18°) and superior ($0.16 \pm 0.07 \mu\text{m}$ at 18°) periphery. The results from the oblique scans ($n = 8$) demonstrated an opposite trend of relative peripheral defocus shift between 45° and 135° meridians. Specifically, the oblique 45° scan showed a gradual increase in relative myopic defocus towards the periphery ($0.10 \pm 0.42 \mu\text{m}$ at 18° infero-nasal and 0.32 ± 0.03

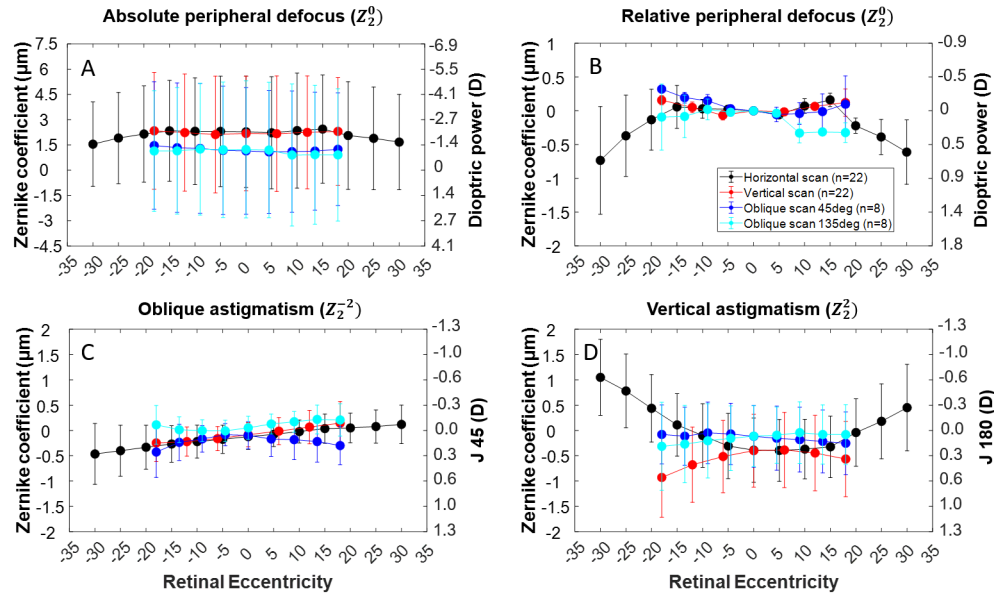


Fig. 4. Peripheral lower-order aberrations (LOAs): A) defocus (Z_2^0); B) defocus relative to the fovea; C) oblique astigmatism (Z_2^{-2}); and D) vertical astigmatism (Z_2^2). The measured aberrations are plotted at four distinct retinal eccentricities: a horizontal (black line, $n = 22$) scan covering $\pm 30^\circ$ from the fovea, a vertical (red line, $n = 22$) scan, and two oblique scans ($n = 8$) along 45° (blue line) and 135° (cyan line), each covering $\pm 18^\circ$ from the fovea. The X-axis displays the degree of retinal eccentricity, with negative values indicating temporal, inferior, infero-temporal, and infero-nasal retinal eccentricities for horizontal, vertical, diagonal 45° , and diagonal 135° scans, respectively. The Y-axis displays the aberration magnitude in microns, while the secondary Y-axis represents the equivalent dioptric power of defocus and astigmatic components (J_0 & J_{45}) for a 5.5 mm pupil. The amplitude scales in A & B differ to better illustrate the absolute and relative defocus distribution across retinal eccentricities. The error bars represent the standard deviation at each eccentricity.

μm at 18° supero-temporal retina), while the 135° scan exhibited relative peripheral hyperopic defocus ($-0.32 \pm 0.15 \mu\text{m}$ at 18° infero-temporal and $-0.09 \pm 0.49 \mu\text{m}$ at 18° supero-nasal retina).

The distribution of astigmatism across the four meridians is illustrated in Figs. 4(C) and (D). Our findings indicate negative vertical astigmatism (Z_2^2) on-axis ($-0.39 \pm 0.63 \mu\text{m}$), which gradually changes to positive Z_2^2 towards the temporal and nasal eccentricities ($0.45 \pm 0.86 \mu\text{m}$ and $1.05 \pm 0.75 \mu\text{m}$, respectively). Interestingly, along the vertical meridian, Z_2^2 showed an opposite trend, becoming more negative towards the inferior ($-0.56 \pm 0.75 \mu\text{m}$) and superior ($-0.93 \pm 0.79 \mu\text{m}$) retina. The oblique scans showed a combination of oblique astigmatism (Z_2^{-2}) and Z_2^2 distribution. The slightly negative on-axis astigmatism ($Z_2^{-2} = -0.10 \pm 0.27 \mu\text{m}$ and $Z_2^2 = -0.16 \pm 0.61 \mu\text{m}$) gradually increased in magnitude to $-0.30 \pm 0.38 \mu\text{m}$ and $-0.25 \pm 0.62 \mu\text{m}$ (Z_2^{-2} & Z_2^2 at 18° infero-nasal retina, respectively) and $-0.43 \pm 0.50 \mu\text{m}$ and $-0.08 \pm 0.58 \mu\text{m}$ (Z_2^{-2} & Z_2^2 at 18° supero-temporal retina, respectively) across the 45° meridional scan. While Z_2^2 maintained a similar trend along the oblique scans, Z_2^{-2} showed a slightly increasing magnitude towards the periphery (relative change from fovea: $0.06 \pm 0.15 \mu\text{m}$ and $0.16 \pm 0.09 \mu\text{m}$ at infero-temporal and supero-nasal 18° retina, respectively). In general, defocus demonstrated a more symmetrical distribution between two eccentricities of each scanning meridian, whereas vertical astigmatism displayed a similar tendency but with a slight asymmetry.

In Fig. 5, the root mean square (RMS) of HOAs and their primary contributors, including vertical (Z_3^{-1}) and horizontal coma (Z_3^1) as well as primary spherical aberration (Z_4^0), are shown. Both the coma components exhibit an asymmetric distribution across retinal eccentricities, with Z_3^1 being dominant across the horizontal meridian and Z_3^{-1} across the vertical meridian. The magnitude of Z_3^1 changes linearly from negative ($-0.33 \pm 0.36 \mu\text{m}$) to positive ($0.35 \pm 0.40 \mu\text{m}$) from temporal to nasal 30° . The magnitude of Z_3^{-1} decreases gradually from $0.17 \pm 0.18 \mu\text{m}$ at inferior 18° eccentricity to $-0.03 \pm 0.28 \mu\text{m}$ at superior 18° eccentricity.

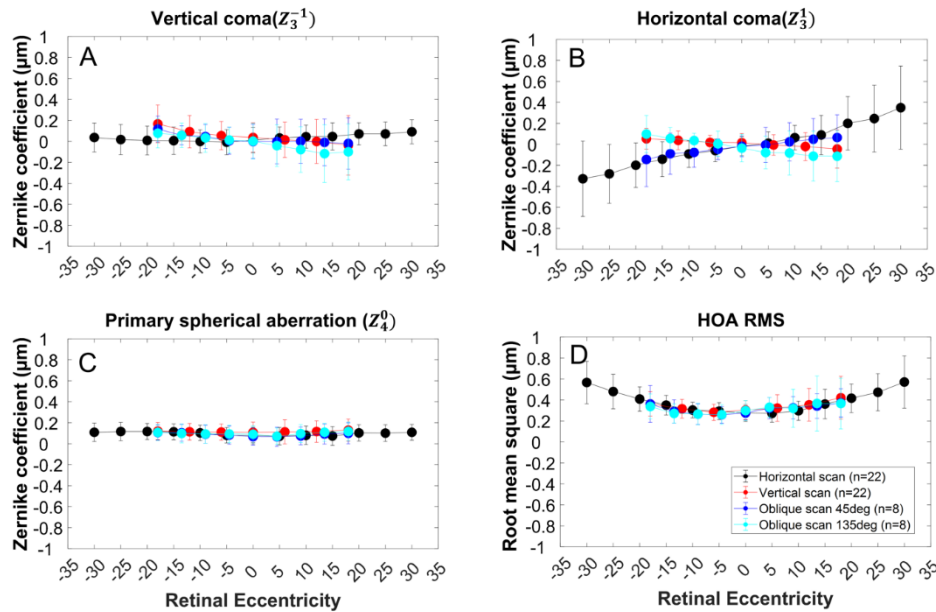


Fig. 5. Higher-order aberrations (HOAs) across the retinal eccentricity: A) vertical coma (Z_3^{-1}); B) horizontal coma (Z_3^1); C) primary spherical aberration (Z_4^0); and D) HOA root-mean-square (RMS). The measured aberrations are plotted at four distinct retinal eccentricities: a horizontal (black line, $n = 22$) scan covering $\pm 30^\circ$ from the fovea, a vertical (red line, $n = 22$) scan, and two oblique scans ($n = 8$) along 45° (blue line) and 135° (cyan line), each covering $\pm 18^\circ$ from the fovea. The X-axis displays retinal eccentricity in degrees, with negative values indicating temporal, inferior, infero-temporal, and infero-nasal retinal eccentricities for horizontal, vertical, diagonal 45° , and diagonal 135° scans, respectively. The Y-axis represents the magnitude of aberrations in microns, calculated for a 5.5 mm pupil size. The error bars represent the standard deviation at each eccentric point.

The distribution of vertical coma also showed changes in the oblique scans towards the periphery, whereas there was negligible change in Z_3^1 . In the oblique 45° scan, Z_3^{-1} changed from a slightly negative magnitude to positive as it progressed from the 18° inferior to 18° superior meridians ($-0.02 \pm 0.25 \mu\text{m}$ to $0.12 \pm 0.12 \mu\text{m}$). Similarly, the oblique 135° scan exhibited a similar trend, with Z_3^{-1} changing from $-0.10 \pm 0.27 \mu\text{m}$ to $0.08 \pm 0.14 \mu\text{m}$ from the inferior to superior 18° eccentricities. The average on-axis primary spherical aberration was $+0.08 \pm 0.08 \mu\text{m}$ and did not exhibit significant variation across peripheral eccentricities. The RMS magnitude of all HOAs increases gradually with eccentricity across all meridians.

Figure 6 presents wavefront maps that were reconstructed using measured Zernike coefficients for a 5.5 mm pupil across various data points from one of the participants in the study. Overall, the aberration distribution across the retina indicated an increasing magnitude of aberrations and a progressively rotationally asymmetric aberration profile with greater retinal eccentricity.

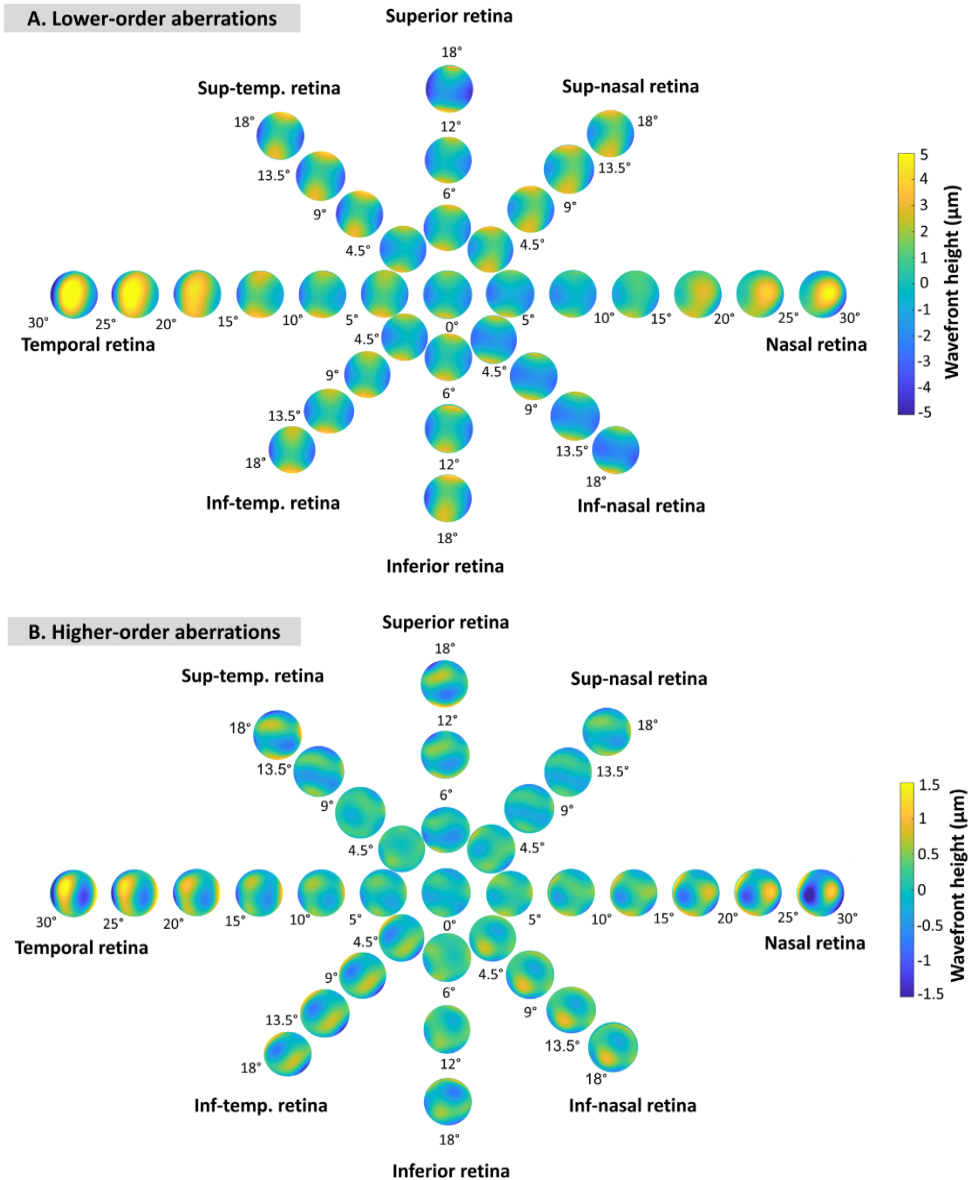


Fig. 6. Pan-retinal schematic representation of wavefront maps reconstructed from the measured aberrations for a 5.5 mm pupil across all four scanning directions. Plot A shows distribution of peripheral lower-order aberrations. Foveal defocus value is subtracted from each retinal location. Plot B shows the distribution of higher-order aberrations. The colormap shows the amplitude of wavefront height in μm .

Figure 6(A) depicts the distribution of peripheral defocus and astigmatism (LOAs) across the measured retinal fields. The horizontal peripheral eccentricity resulted in a more significant shift in astigmatism and defocus than other meridians due to the larger scanning range across the nasal and temporal eccentricities. Figure 6(B) shows the distribution of HOAs, which revealed asymmetric aberration patterns, particularly across the horizontal meridian and inferior retinal locations. These trends were consistent in other study participants with the mean results presented in Fig. 5, indicating a trend of negative to positive horizontal coma across the horizontal meridian from temporal to nasal retina.

4. Discussion

We have developed a novel wavefront sensor that is capable of scanning a wide range of eccentricities across any retinal meridian in less than 5 seconds. The multi-directionality of the device is attained by way of a unique scanning method that involves the concurrent operation of horizontal and vertical rotational motors (R1 and G1 in Fig. 2) and allows measurement of a wide retinal meridian within a single blink interval. Additionally, the system is designed for natural eye fixation at the primary gaze, rather than relying on off-axis fixation to align the system to the subject's eye. This paper details the successful demonstration of measuring aberrations of human eyes along the horizontal, vertical, and two oblique meridians.

The performance of the WSWS has been validated and on-eye aberration measurement was performed on 22 young individuals, having different refractive errors (mean spherical equivalent \pm SD: -1.98 ± 3.06 D). The results indicated a gradual decrease with eccentricity in the defocus component towards the temporal and nasal periphery, reflecting a relative peripheral hyperopic shift. To better understand the peripheral relative defocus distribution, we have further grouped our subjects into myopic (-4.94 ± 1.46 D, $n = 10$) and non-myopic (0.48 ± 1.25 D, $n = 12$) categories based on their foveal refraction. Subjects with foveal spherical equivalent equal to or more negative than -0.75 D were categorized as myopic. Figure 7 reveals the myopic group had relative peripheral hyperopia, whereas non-myopic subjects had relative peripheral near-emmetropic to slightly myopic defocus. These findings along the horizontal retinal eccentricities are in agreement with previous studies [13–18].

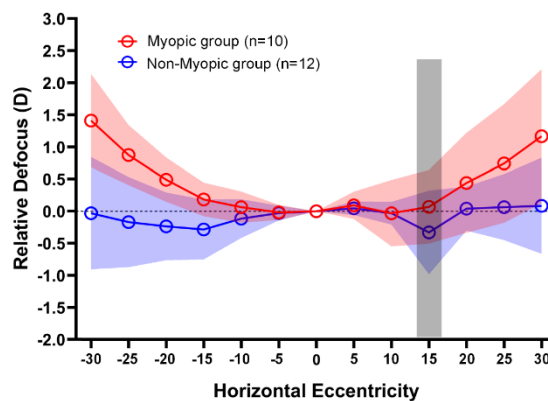


Fig. 7. Average relative defocus (D) across the horizontal meridian (in degrees) in the myopic (red) and non-myopic (blue) groups. The shaded red and blue areas represent the standard deviation at each retinal eccentricity. Positive values on the X-axis indicate the nasal retina, and the thick gray vertical bar denotes the area affected by the optic disc.

Previous studies have reported a pan-retinal defocus distribution with a contrasting trend along different meridians [52,53], which is also in line with our results from multidirectional

scans (Figs. 4 and 6). In addition to defocus, we have observed a trend of bidirectional change of vertical astigmatism (Z_2^2) along the horizontal and vertical eccentricities. Previous studies have reported similar distributions of astigmatism along the horizontal and vertical meridians [13,49,54–56]. Furthermore, we have observed a similar trend in oblique astigmatism (Z_2^{-2}) along the diagonal meridians.

Among our study participants, the root mean square (RMS) of HOAs increases as retinal eccentricity increases. This is mainly due to the influence of vertical coma (Z_3^{-1}) and horizontal coma (Z_3^1). Our analysis of horizontal scans indicated a linear change in Z_3^1 magnitude, ranging from negative to positive values from temporal to nasal retinal eccentricities (Fig. 5(B)). Meanwhile, the vertical meridional scan revealed that Z_3^{-1} was the dominant component, changing from a positive to negative coefficient from inferior to superior retinal locations. This observation is well documented, especially across the horizontal and vertical meridians [54]. The average on-axis Z_4^0 reported as $0.14 \mu\text{m}$ for 5.8 mm pupil in a large-population study [57], which is close to the on-axis mean Z_4^0 in our study participants ($+0.08 \pm 0.08 \mu\text{m}$, measured over 5.5 mm pupil). The Z_4^0 term exhibits minimal change across the peripheral retinal locations, which is supported by earlier reports but limited to horizontal and vertical eccentricities [54]. The consistency of obtained LOA and HOA across the measured field with relevant literature proves efficacy of our system's on-eye performance.

The relationship between HOAs and eye growth remains uncertain due to conflicting results reported in the literature. Some studies have found no differences in central or peripheral HOAs between myopic and non-myopic refractive groups, [58–63] while significant differences have been found in other studies. [59,64–66] We performed sub-group analysis on HOA (for 5.5 mm pupil) using the same grouping criteria, as previously described for Fig. 7. Figure 8 shows trends of HOA RMS for the two groups in our study. Average foveal RMS values were identical between myopic ($0.28 \pm 0.13 \mu\text{m}$) and non-myopic subjects ($0.28 \pm 0.10 \mu\text{m}$). Peripheral RMS increased with horizontal retinal eccentricities for both groups, where myopic subjects exhibited higher values compared to non-myopic subjects. The most dominant HOA contributing to these trends was Z_3^1 . Despite this interesting observation, no statistically meaningful group difference was found due to large inter-subject variability and small sample sizes per group.

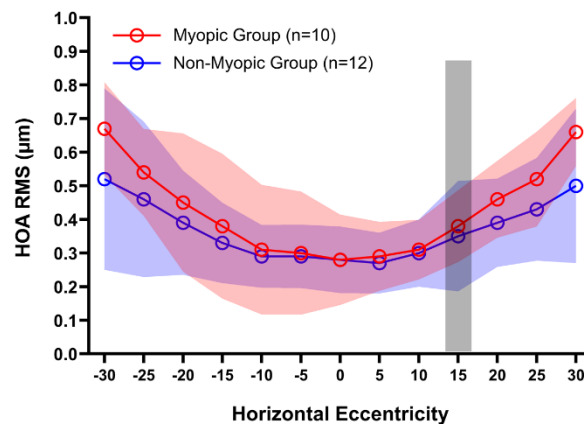


Fig. 8. Average higher-order aberration RMS (for 5.5 mm pupil) across the horizontal meridian (in degrees) in the myopic (red) and non-myopic (blue) groups. The shaded red and blue areas represent the standard deviation at each retinal eccentricity. Positive values on the X-axis indicate the nasal retina, and the thick gray vertical bar denotes the area affected by the optic disc.

Recently, there has been a significant focus on the study of peripheral aberrations, particularly in the area of myopia. Peripheral aberration measurement devices have been previously attempted using several approaches. Wei and Thibos used a double-pass optical system to develop a scanning SH aberrometer. [47] Scanning in their system was achieved using 2 scanning mirrors, which redirect the light beam to 37 discrete measurement points located in a grid of $\pm 15^\circ$ visual field within 7 seconds. This setup allows the instrument to use primary gaze fixation during wavefront measurement, however, measurements were limited to a relatively small field. An alternate approach was used in The BHVI-EyeMapper, employing an SH wavefront sensor that features a complex system of 33 fixed mirrors and one scanning mirror. [48] This sensor can measure the horizontal retinal eccentricity up to $\pm 50^\circ$ in increments of 10 degrees within 0.5 seconds while maintaining central fixation. However, it is important to note that while this sensor is speedy and can cover a wide field, it is limited to discrete retinal locations only along the horizontal axis. Jaeken B et al. [46] built a SH peripheral wavefront sensor with a wide-field horizontal scanning capability. It can scan $\pm 40^\circ$ horizontally and provides 81 high-resolution images in 1.8 seconds. Their scanning device is fast and capable to measure aberration at every 1° interval, however, was limited to the horizontal scan only. Although these innovations are exciting, they still have limitations, such as a smaller scanning range, limited to one meridian, or requiring eccentric fixation through ocular rotation or head turn. Recently, a whole-field peripheral refractor has been developed that estimates refraction in a circular retinal patch of $\pm 25^\circ$ from central fixation within three seconds [49]. This new approach has promising implications for scanning across all meridians without exposing an external scanning mechanism. However, it has limitations such as being incapable of measuring higher-order aberrations and a lack of an open view fixation system.

Previous peripheral wavefront sensors have had difficulties with achieving automatic and low-cost vertical scanning in a small footprint. Our approach of implementing a motorized goniometer overcame these limitations and enabled us to perform multidirectional scans rapidly while maintaining natural central fixation as the primary gaze. Moreover, this capability expands the applications of aberration quantification to include contact lens-induced peripheral aberration assessment, which is essential for development of more effective corrective lenses for myopia control. The usage of primary gaze fixation is crucial in this discipline to avoid unwanted contact lens decentration with eccentric fixations. Furthermore, natural primary fixation allows for a more comfortable measurement procedure, from the subject's perspective, which may allow the inclusion of subjects such as children. Again, quantifying peripheral aberrations in children is crucial in gaining a better understanding of how ocular optics contribute to emmetropization and ocular development.

Although we have successfully constructed a novel scanning wavefront system, there are some areas of improvement that could be ameliorated in future WSWS designs. Firstly, corneal reflection of the light source from the anterior corneal surface at scanning angles close to on-axis caused interference with Zernike analysis. This can be avoided by slightly dislocating the laser beam from the corneal apex, however, that may also cause a similarly sized offset between expected and actual scanning angle. The optical design could further be improved with the implementation of a longer wavelength light source that is completely invisible to the human eye. The current design uses near infrared light which is still visible and may interrupt fixation during scanning. Another limitation is the portability of the device. The current WSWS is limited to laboratory research applications due to its size and design. Furthermore, the large commercial goniometer limited the scanning range of the system, especially for oblique meridians. A compact portable peripheral wavefront sensing device could expand possible applications of the WSWS to include high throughput data collection in clinics or schools. This kind of flexibility could also enable longitudinal experiments, which are critical for untangling the underlying mechanisms of visual-driven processes such as myopia development and progression.

In summary, the present work describes the development of a novel wavefront sensor that can scan any area of the retina across a wide range and uses a distinctive scanning method with multidirectional capability. The system is optimized for natural eye fixation at the primary gaze, eliminating the requirement for eccentric fixation during peripheral aberration measurement. Its performance has been evaluated in 22 young subjects, demonstrating precise peripheral measurement of both LOAs and HOAs. The open-view natural fixation mechanism has important implications for measuring peripheral optics in both children and adults, particularly in studying myopia.

Funding. Research to Prevent Blindness; National Institutes of Health (R01EY014999, R01EY034151).

Acknowledgments. We thank Mr. Keith Parkins at the Center for Visual Science, University of Rochester for building the WSWs control software. We are also thankful to all the study participants.

Disclosures. The authors declare no conflicts of interest.

Data availability. The data presented in this paper are not publicly available but may be obtained from the authors upon request.

References

1. A. R. Rudnicka, V. V. Kapetanakis, A. K. Wathern, N. S. Logan, B. Gilmartin, P. H. Whincup, D. G. Cook, and C. G. Owen, "Global variations and time trends in the prevalence of childhood myopia, a systematic review and quantitative meta-analysis: Implications for aetiology and early prevention," *Br. J. Ophthalmol.* **100**(7), 882–890 (2016).
2. B. A. Holden, T. R. Fricke, D. A. Wilson, M. Jong, K. S. Naidoo, P. Sankaridurg, T. Y. Wong, T. J. Naduvilath, and S. Resnikoff, "Global Prevalence of Myopia and High Myopia and Temporal Trends from 2000 through 2050," *Ophthalmology* **123**(5), 1036–1042 (2016).
3. M. Mehdizadeh and H. Ashraf, "Prevalence of Cataract Type in Relation to Axial Length in Subjects with High Myopia and Emmetropia in an Indian Population," *Am. J. Ophthalmol.* **146**(2), 329–330 (2008).
4. I. Dragoumis, A. Richards, P. Alexander, A. Poulson, and M. Snead, "Retinal detachment in severe myopia," *Lancet* **390**(10090), 124 (2017).
5. P. J. Polkinghorne and J. P. Craig, "Northern New Zealand Rhegmatogenous Retinal Detachment Study: epidemiology and risk factors," *Clin. Exp. Ophthalmol.* **32**(2), 159–163 (2004).
6. X. Li and Beijing Rhegmatogenous Retinal Detachment Study Group, "Incidence and epidemiological characteristics of rhegmatogenous retinal detachment in Beijing, China," *Ophthalmology* **110**(12), 2413 (2003).
7. J. Vongphanit, P. Mitchell, and J. J. Wang, "Prevalence and progression of myopic retinopathy in an older population," *Ophthalmology* **109**(4), 704–711 (2002).
8. T. Blue and M. Eye, "The Relationship between Glaucoma and myopia," **117**, 2010–2015 (2010).
9. M. Qiu, S. Y. Wang, K. Singh, and S. C. Lin, "Association between myopia and glaucoma in the united states population," *Investig. Ophthalmol. Vis. Sci.* **54**(1), 830–835 (2013).
10. F. Rempt, J. Hoogerheide, and W. P. . Hoogenboom, "Peripheral retinoscopy and the skiagram," *Ophthalmologica* **162**(1), 1–10 (1971).
11. H. W. Hoogerheide J and F Rempt, "Acquired miopia in young pilots," *Ophthalmology* **163**(4), 209 (1971).
12. E. L. Smith, R. Ramamirtham, Y. Qiao-Grider, L. F. Hung, J. Huang, C. S. Kee, D. Coats, and E. Paysse, "Effects of foveal ablation on emmetropization and form-deprivation myopia," *Investig. Ophthalmol. Vis. Sci.* **48**, 3914–3922 (2007).
13. D. A. Atchison, N. Pritchard, and K. L. Schmid, "Peripheral refraction along the horizontal and vertical visual fields in myopia," *Vision Res.* **46**(8-9), 1450–1458 (2006).
14. M. Millodot, "Effect of ametropia on peripheral refraction," *Am J Optom Physiol Opt.* **58**, 691 (1981).
15. N. S. Logan, B. Gilmartin, C. F. Wildsoet, and M. C. M. Dunne, "Posterior retinal contour in adult human anisomyopia," *Invest. Ophthalmol. Visual Sci.* **45**(7), 2152–2162 (2004).
16. L. A. Jones-Jordan, L. T. Sinnott, S. A. Cotter, R. N. Kleinstein, R. E. Manny, D. O. Mutti, J. Daniel Twelker, and K. Zadnik, "Time outdoors, visual activity, and myopia progression in juvenile-onset myopes," *Invest. Ophthalmol. Visual Sci.* **53**(11), 7169–7175 (2012).
17. D. O. Mutti, R. I. Sholtz, N. E. Friedman, and K. Zadnik, "Peripheral refraction and ocular shape in children," *Invest. Ophthalmol. Visual Sci.* **41**, 1022–1030 (2000).
18. A. Seidemann, F. Schaeffel, A. Guirao, N. Lopez-Gil, and P. Artal, "Peripheral refractive errors in myopic, emmetropic, and hyperopic young subjects," *J. Opt. Soc. Am. A* **19**(12), 2363 (2002).
19. E. L. S. Iii, C. Kee, R. Ramamirtham, Y. Qiao-grider, and L. Hung, "Peripheral vision can influence eye growth and refractive development in infant monkeys," *Invest. Ophthalmol. Visual Sci.* **46**, 1 (2005).
20. E. L. Smith, L. F. Hung, and J. Huang, "Relative peripheral hyperopic defocus alters central refractive development in infant monkeys," *Vision Res.* **49**(19), 2386–2392 (2009).
21. W. Neil Charman and H. Radhakrishnan, "Peripheral refraction and the development of refractive error: A review," *Ophthalmic Physiol. Opt.* **30**(4), 321–338 (2010).

22. R. Schippert and F. Schaeffel, "Peripheral defocus does not necessarily affect central refractive development," *Vision Res.* **46**(22), 3935–3940 (2006).
23. C. C. A. Sng, X. Y. Lin, G. Gazzard, B. Chang, M. Dirani, L. Lim, P. Selvaraj, K. Ian, B. Drobe, T. Y. Wong, and S. M. Saw, "Change in peripheral refraction over time in Singapore Chinese children," *Invest. Ophthalmol. Visual Sci.* **52**(11), 7880–7887 (2011).
24. D. A. Atchison, S. M. Li, H. Li, S. Y. Li, L. R. Liu, M. T. Kang, B. Meng, Y. Y. Sun, S. Y. Zhan, P. Mitchell, and N. Wang, "Relative peripheral hyperopia does not predict development and progression of myopia in children," *Invest. Ophthalmol. Visual Sci.* **56**(10), 6162–6170 (2015).
25. D. O. Mutti, L. T. Sinnott, G. L. Mitchell, L. A. Jones-Jordan, M. L. Moeschberger, S. A. Cotter, R. N. Kleinstein, R. E. Manny, J. D. Twelker, and K. Zadnik, "Relative peripheral refractive error and the risk of onset and progression of myopia in children," *Invest. Ophthalmol. Visual Sci.* **52**(1), 199–205 (2011).
26. B. Jaeken and P. Artal, "Optical quality of emmetropic and myopic eyes in the periphery measured with high-angular resolution," *Invest. Ophthalmol. Visual Sci.* **53**(7), 3405–3413 (2012).
27. A. Benavente-Pérez, A. Nour, and D. Troilo, "Axial eye growth and refractive error development can be modified by exposing the peripheral retina to relative myopic or hyperopic defocus," *Invest. Ophthalmol. Visual Sci.* **55**(10), 6765–6773 (2014).
28. E. L. Smith, "Prentice Award Lecture 2010: a case for peripheral optical treatment strategies for myopia," *Optom. Vis. Sci.* **88**(9), 1029–1044 (2011).
29. J. Pauné, H. Morales, J. Armengol, L. Quevedo, M. Faria-Ribeiro, and J. M. González-Méijome, "Myopia control with a novel peripheral gradient soft lens and orthokeratology: a 2-year clinical trial," *Biomed Res. Int.* **2015**, 1 (2015).
30. P. Sankaridurg, B. Holden, E. Smith, T. Naduvilath, X. Chen, P. L. de la Jara, A. Martinez, J. Kwan, A. Ho, K. Frick, and J. Ge, "Decrease in rate of myopia progression with a contact lens designed to reduce relative peripheral hyperopia: One-year results," *Invest. Ophthalmol. Visual Sci.* **52**(13), 9362–9367 (2011).
31. J. J. Walline, K. L. Greiner, M. E. McVey, and L. A. Jones-Jordan, "Multifocal contact lens myopia control," *Optom. Vis. Sci.* **90**(11), 1207–1214 (2013).
32. Q. Ji, Y. S. Yoo, H. Alam, and G. Yoon, "Through-focus optical characteristics of monofocal and bifocal soft contact lenses across the peripheral visual field," *Ophthalmic Physiol. Opt.* **38**(3), 326–336 (2018).
33. K. Baskaran, R. Rosén, P. Lewis, P. Unsbo, and J. Gustafsson, "Benefit of adaptive optics aberration correction at preferred retinal locus," *Optom. Vis. Sci.* **89**(9), 1417–1423 (2012).
34. P. Lewis, A. P. Venkataraman, and L. Lundström, "Contrast Sensitivity in Eyes with Central Scotoma: Effect of Stimulus Drift," *Optom. Vis. Sci.* **95**(4), 354–361 (2018).
35. S. Ortiz-Peregrina, M. Casares-López, J. J. Castro-Torres, R. G. Anera, and P. Artal, "Effect of peripheral refractive errors on driving performance," *Biomed. Opt. Express* **13**(10), 5533 (2022).
36. C. Vater, B. Wolfe, and R. Rosenholtz, "Peripheral vision in real-world tasks: A systematic review," *Psychon. Bull. Rev.* **29**(5), 1531–1557 (2022).
37. A. P. Venkataraman, R. Rosén, A. A. Heredia, P. Piers, C. C. Vidal, and L. Lundström, "Peripheral vision and hazard detection with average phakic and pseudophakic optical errors," *Biomed. Opt. Express* **12**(6), 3082 (2021).
38. E. A. Villegas, J. M. Marín, H. Ginis, C. Robles, E. Alcón, L. Hervella, P. M. Prieto, P. Taña-Rivero, and P. Artal, "Peripheral refraction and contrast detection sensitivity in pseudophakic patients implanted with a new meniscus intraocular lens," *J. Refract. Surg.* **38**(4), 229–234 (2022).
39. D. A. Atchison, A. Mathur, S. A. Read, M. I. Walker, A. R. Newman, P. P. Tanos, R. T. McLennan, and A. H. Tran, "Peripheral ocular aberrations in mild and moderate keratoconus," *Invest. Ophthalmol. Visual Sci.* **51**(12), 6850–6857 (2010).
40. A. P. Venkataraman, P. Papadogiannis, D. Romashchenko, S. Winter, P. Unsbo, and L. Lundström, "Peripheral resolution and contrast sensitivity: effects of monochromatic and chromatic aberrations," *J. Opt. Soc. Am. A* **36**(4), B52 (2019).
41. K. Sapkota, J. Gomes, and S. Franco, "Effect of accommodation on peripheral higher order aberrations," *Photonics* **9**(2), 64 (2022).
42. A. Mathur, J. Gehrmann, and D. A. Atchison, "Pupil shape as viewed along the horizontal visual field," *J. Vis.* **13**(6), 3 (2013).
43. D. A. Atchison, "Comparison of peripheral refractions determined by different instruments," *Optom. Vis. Sci.* **80**(9), 655–660 (2003).
44. J. Tabernero and F. Schaeffel, "More irregular eye shape in low myopia than in emmetropia," *Invest. Ophthalmol. Visual Sci.* **50**(9), 4516–4522 (2009).
45. D. A. Atchison and D. H. Scott, "Monochromatic aberrations of human eyes in the horizontal visual field," *J. Opt. Soc. Am. A* **19**(11), 2180 (2002).
46. B. Jaeken, L. Lundström, and P. Artal, "Fast scanning peripheral wave-front sensor for the human eye," *Opt. Express* **19**(8), 73–82 (2011).
47. X. Wei and L. Thibos, "Design and validation of a scanning Shack Hartmann aberrometer for measurements of the eye over a wide field of view," *Opt. Express* **18**(2), 1134 (2010).
48. C. Fedtke, K. Ehrmann, D. Falk, R. C. Bakaraju, and B. A. Holden, "The BHVI-eyemapper: Peripheral refraction and aberration profiles," *Optom. Vis. Sci.* **91**(10), 1199–1207 (2014).

49. E. J. Fernandez, S. Sager, Z. Lin, J. H. Hao, J. Roca, P. M. Pedro, Z. Yang, W. Lan, and P. Artal, "Instrument for fast whole-field peripheral refraction in the human eye," *Biomed. Opt. Express* **13**(5), 2947–2959 (2022).
50. American National Standards Institute. (2014). Safe Use of Lasers (ANSI Z136.1-2014). Section 4.4.2.2: Maximum Permissible Exposure (MPE) for Ocular Exposure. New York, NY: Laser Institute of America. (n.d.).
51. L. Lundström, J. Gustafsson, and P. Unsbo, "Population distribution of wavefront aberrations in the peripheral human eye," *J. Opt. Soc. Am. A* **26**(10), 2192 (2009).
52. M. G. García, D. Pusti, S. Wahl, and A. Ohlendorf, "A global approach to describe retinal defocus patterns," *PLoS One* **14**, 1–13 (2019).
53. S. Wang, Z. Lin, X. Xi, Y. Lu, L. Pan, X. Li, P. Artal, W. Lan, and Z. Yang, "Two-Dimensional, High-Resolution Peripheral Refraction in Adults with Isomyopia and Anisomyopia," *Invest. Ophthalmol. Visual Sci.* **61**(6), 16 (2020).
54. D. Romashchenko, R. Rosén, and L. Lundström, "Peripheral refraction and higher order aberrations," *Clin. Exp. Optom.* **103**(1), 86–94 (2020).
55. L. Zheleznyak, "Peripheral optical anisotropy in refractive error groups," *Ophthalmic Physiol. Opt.* **43**(3), 1–10 (2023).
56. D. A. Atchison, "Optical models for human myopic eyes," *Vision Res.* **46**(14), 2236–2250 (2006).
57. J. Porter, A. Guirao, I. G. Cox, and D. R. Williams, "Monochromatic aberrations of the human eye in a large population," *J. Opt. Soc. Am. A* **18**(8), 1793 (2001).
58. J. Gomes, K. Sapkota, and S. Franco, "Central and peripheral ocular high-order aberrations and their relationship with accommodation and refractive error: a review," *Vision* **7**(1), 19 (2023).
59. J.-A. Little, S. J. McCullough, K. M. M. Breslin, and K. J. Saunders, "Higher order ocular aberrations and their relation to refractive error and ocular biometry in children," *Invest. Ophthalmol. Visual Sci.* **55**(8), 4791–4800 (2014).
60. A. A. Martinez, P. R. Sankaridurg, T. J. Naduvilath, and P. Mitchell, "Monochromatic aberrations in hyperopic and emmetropic children," *J. Vis.* **9**(1), 23 (2009).
61. D. Thapa, A. Fleck, V. Lakshminarayanan, and W. R. Bobier, "Ocular wavefront aberration and refractive error in pre-school children," *J. Mod. Opt.* **58**(19-20), 1681–1689 (2011).
62. S. Yazar, A. W. Hewitt, H. Forward, C. M. McKnight, A. Tan, J. A. Mountain, and D. A. Mackey, "Comparison of monochromatic aberrations in young adults with different visual acuity and refractive errors," *J. Cataract Refract. Surg.* **40**(3), 441–449 (2014).
63. F. Karimian, S. Feizi, and A. Doozande, "Higher-order aberrations in myopic eyes," *J. Ophthalmic Vis. Res.* **5**, 3–9 (2010).
64. U. L. Osuagwu, M. Suheimat, and D. A. Atchison, "Peripheral aberrations in adult hyperopes, emmetropes and myopes," *Ophthalmic Physiol. Opt. J. Br. Coll. Ophthalmic Opt.* **37**(2), 151–159 (2017).
65. T. Li, X. Zhou, Z. Chen, X. Zhou, R. Chu, and M. R. Hoffman, "Relationship between ocular wavefront aberrations and refractive error in Chinese school children," *Clin. Exp. Optom.* **95**(4), 399–403 (2012).
66. X. U. Cheng, A. Bradley, X. I. N. Hong, and L. N. Thibos, "Relationship between Refractive Error and Monochromatic Aberrations of the Eye," *Optom. Vis. Sci.* **80**(1), 43 (2003).